An Edge-Region Force Guided Active Shape Approach for Automatic Lung Field Detection in Chest Radiographs

Tao Xu[a], Mrinal K. Mandal[a], Richard Long[b], Irene Cheng[c], Anup Basu[c]

[a] Department of Electrical and Computer Engineering, University of Alberta, Edmonton, Alberta, Canada, T6G 2V4   Tel: 1-780-492-0294   Email: tx1@ualberta.ca mandal@ece.ualberta.ca

[b] Division of Pulmonary Medicine Departments of Medicine, University of Alberta, Edmonton, Alberta, Canada, T6G 2V2   Tel: 1-780-407-1427   Fax: 1-780-407-1429   Email: richard.long@ualberta.ca

[c] Department of Computing Science, University of Alberta, Edmonton, Alberta, Canada, T6G 2E8   Tel: 1-780-492-3330   Fax: 1-780-492-1071   Email: locheng@ualberta.ca basu@ualberta.ca

Corresponding Author: Anup Basu Email: basu@ualberta.ca

Abbreviated title: Edge-Region Force Guided Lung Field Segmentation

ABSTRACT

Automatic and accurate lung field segmentation is an essential step for developing an automated computer-aided diagnosis system for chest radiographs. Although active shape model (ASM) has been useful in many medical imaging applications, lung field segmentation remains a challenge due to the superimposed anatomical structures. We propose an automatic lung field segmentation technique to address the inadequacy of ASM in lung field extraction. Experimental results using both normal and abnormal chest radiographs show that the proposed technique provides better performance and can achieve 3-6 % improvement on accuracy, sensitivity and specificity compared to traditional ASM techniques.

Key Words: Computer-Aided Diagnosis, Chest Radiograph, Edge and Region Force, Active Shape Model, Poisson Inverse Gradient, Shape Priors, Level Set

1. INTRODUCTION

Although encouraging results are obtained from using computed tomography (CT) and positron emission tomography (PET) to diagnose respiratory diseases, particularly lung cancer [1-2], chest radiography still remains the most commonly used procedure making up more than one third of all examinations in a typical radiology department [3] for several reasons. First, using chest radiography provides a noninvasive mean to reveal unsuspected pathologic alterations. Second, it has lower radiation dose and lower cost than CT. Also, chest X-ray machines are more accessible, especially in developing countries[4]. Therefore, chest radiography is often the first and likely the only diagnostic imaging test performed on patients known to have or suspected of having a thoracic abnormality. Given the shortage of radiologists compared to the large amount of chest radiographs that need to be examined, our research focus is on supporting a computer-aided diagnosis (CAD) system in chest radiography to reduce the backlog by filtering off less severe cases, so that radiologists can dedicate their limited resources efficiently on infectious cases.

Many clinical studies were conducted to evaluate the performance of CAD on detecting different lung diseases. In 2009, researchers from the University of Maryland Medical Centre reported that CAD software could help identify approximately half of previously missed lung cancer lesions in chest X-ray images. However, there was a significant trade-off between discovering more potential targets and low false positive rates[43]. The performance of a CAD algorithm in the detection of pulmonary nodules on tomography images was evaluated in 2007 and it was found that CAD could detect a substantial number of nodules unseen by radiologists [44]. In 2010, another research finding suggested that the result produced by

a CAD system in identifying lung cancers was similar to that of radiologists experienced with CT

screening[45]. A CAD procedure in chest radiography involves various steps including lung field

segmentation, feature extraction and analysis. Since only the information inside the lung is required,

automatic lung field segmentation becomes a mandatory pre-processing step for computerized analysis of

chest radiographs. Accurate segmentation results will provide useful information for the later feature

extraction and analysis steps. Our contributions lie in developing an automatic and accurate lung field

segmentation technique in chest radiographs. A robust lung field segmentation technique, accurately

isolating the target region from the background, will reduce the high false positive rates [43].

Previous efforts on lung field segmentation approaches can be classified into two categories: low level

and high level methods. Low level methods focus on pixels and edges, such as thresholding, edge detection

and linking, and pixel-based classification or clustering, to guide segmentation. For example, Armato et

al.[5] used a combination of gray-level thresholding and contour smoothing for lung field segmentation.

Duryea et al.[6] proposed a heuristic edge tracing approach to extract lung regions. McNitt-Gray et al.[7]

developed a method using feature-based classification of pixels for segmenting the lung. Shi et al.[8]

proposed a Gaussian kernel-based fuzzy clustering algorithm with spatial features for automatic lung field

segmentation. These techniques without prior knowledge are usually fast and automatic but often not

reliable due to the variability that exists in an image, *e.g.*, abnormal anatomy and poor image quality.

High level methods, on the other hand, try to utilize the prior knowledge of generic thoracic images to

overcome the shortcomings of the low level methods. Two types of high level methods have been applied

on lung field segmentation. The first type is knowledge-based model matching techniques. For example,

Brown et al.[9] developed a knowledge-based system which matches image edges to a lung boundary

model. This knowledge-based method was later refined by Park et al. [10] and Luo et al. [11]. However, local features used for matching the model are derived from low-level techniques which may not accurately correspond to the model.

Another type of high level methods is active contours incorporated with shape priors. An example of active contour techniques is level-set with shape priors (LSSP). Three types of LSSP have been successfully applied into different medical imaging modalities: edge-based LSSP, region-based LSSP, and hybrid (both edge and region-based) LSSP. For example, Leventon et al.[37] first incorporated shape priors into the edge-guided geodesic active contours (GAC) using level-set. These techniques are sensitive to image noise and weak edges. Tsai et al.[38] proposed to combine the shape constraint into the Chan and Vese (CV) model [39] to overcome the drawbacks of edge-based LSSP. However, the CV model's assumption (foreground and background regions are statistically homogenous) causes these methods to fail when segmenting images with intensity inhomogeneity. Appropriate computation of foreground and background in local regions need to be considered [40]. Bresson et al.[41] finally consolidated the GAC and CV models with shape priors under the level set framework. Similar hybrid LSSP [42] is proposed for lung segmentation by considering specific image features in chest radiographs, in which the region related energy term assumes the foreground and background regions follow the Gaussian distribution, and the edge related energy term combines the low level canny edge map and castrophenic angle corner feature. The hybrid LSSP techniques and the edge-based and region-based LSSP compensate each other, but increases the complexity, such as higher computational cost and more parameters to adjust (e.g., weights of edge, region and shape related energy terms). More discussion on LSSP can be found in the Appendix.

Active contours of snake and active shape model (ASM) have achieved more popularity for lung field

segmentation in recent years. Iglesias et al. [12] first introduced the snake with shape constraint for

detecting lung contours, and studied the influence of the different parameters of the snake. Yu et al.[13]

derived the nonlinear shape statistics which were used for shape regularization in snake. Nevertheless,

snake suffers from sensitivity to parameters selection and limitation of one object segmentation. ASM was

then proposed by Cootes et al.[18] to overcome these problems. Ginneken et al.[14] applied an ASM with

optimal texture features for lung field segmentation based on machine learning. Shi et al.[15] combined the

local scale invariant feature transform (SIFT) feature to the ASM for detecting lung field. Iakovidis et al.[16]

applied ASM supported by selective thresholding for detecting lung boundaries in portable chest

radiographs. Although ASM-based techniques have achieved satisfactory segmentation results, these

techniques focus on exploiting local features and thus can fail to locate global features. Without global

regulation and given the superimposed anatomical structures on chest radiographs, shape restrictions plus

local features alone are unable to achieve optimal segmentation [17]. Hence, satisfactory convergence relies

very much on how close their initialization is to the actual lung field contour. To overcome this initialization

problem, a user-guided manual initialization is used in the typical ASM[18], making this method

supervised and not automatic. Cootes et al. [19] proposed a multi-resolution approach, which could extend

the search to include points farther away but still within a certain distance limit. Brejl et al. [20] used an

exhaustive search for those situations in which the object might be located anywhere in the image. Specific

features such as intensity feature introduced by Li et al. [21] and color feature introduced by Mahoor et al.

[22] are used for automatic initialization, but these techniques are task-specific. Cosio[23] proposed a more

complex automatic ASM which combines pixel classification with a multi-population genetic algorithm.

Similar to the exhaustive search, the computational cost is very expensive. We have included a detailed

comparison in the Appendix, which shows that the better performance of ASM over level-set techniques on lung field segmentation in chest radiographs is not because the parameter setting has been selected incorrectly, but due to some characteristics of the methods.

In this paper, we propose an efficient automatic segmentation technique for lung boundary detection in chest radiographs. The proposed method applies the global edge and region force (ERF) field, which makes the *automatic initialization and segmentation stages* of the CAD framework more robust. Experimental results show that our method significantly improves the typical ASM[18] and performs better than the hybrid LSSP [42] segmentation methods in terms of accuracy, sensitivity and specificity, as well as time efficiency.

The rest of this paper is organized as follows. Section 2 gives the model formulation. Section 3 describes the proposed method in detail. Section 4 reports and analyzes experimental results. Discussion and Conclusions are presented in Section 5 and Section 6 respectively.

2. MODEL FORMULATION

Typical ASM, which requires supervision to adjust certain parameters, is composed of three major stages: shape learning, initialization (often manual) and segmentation (Fig. 1). These stages are described below.

2.1 Shape Learning Stage

In this stage, the shape prior and the gray level pattern of the objects are learnt by statistically analyzing the training image dataset. These two learning tasks are executed by shape model generation and

gray level appearance model (GLAM) generation.

2.1.1 Shape Model Generation

A deformable shape model is computed from the manually annotated shapes on M training images. Assuming that the object shape on the ith image is denoted by $\hat{C}^i$ and each shape has N points (henceforth referred to as the landmark points), $\hat{C}^i$ can then be represented as:

$$\hat{C}^i = \left\{ (\hat{x}_1^i, \hat{y}_1^i), (\hat{x}_2^i, \hat{y}_2^i), ... (\hat{x}_N^i, \hat{y}_N^i) \right\}, \quad i = 1, 2, ... M. \tag{1}$$

After aligning different shapes by using Generalized Procrustes Analysis [24], Principal Component Analysis (PCA) is performed to approximate any shape in the training set as follows:

$$C^i \approx \overline{C} + P_k b_k^i \tag{2}$$

where $\overline{C}$ denotes the mean shape, $P_k = [p_1, p_2, ... p_k]$ corresponds to the first k eigenvectors, and $b_k^i = [b_1, b_2, ... b_k]^T$ is a vector of weights that defines the shape parameters. By allowing a variation range of shape parameters, this method ensures the gross similarity among shapes.

2.1.2. Gray Level Appearance Model Generation

PCA is similarly applied to characterize the gray level pattern around each landmark point. In the typical ASM method, only a 1-D profile along the normal direction of the landmark point is considered. The GLAM of the landmark point j in the ith image can be approximated as:

$$z_j^i \approx \overline{z_j} + P_z b_z^i \tag{3}$$

where $\overline{z_j}$ denotes the mean gradient profile along each point's normal direction, P_z is a matrix consisting of

significant modes of gray level variations, and b_z is a vector of weights that defines the gray level parameters. Note that although being standard in the typical ASM framework, the underlying assumption of a normal profile distribution often does not hold. Thus, optimal local features based on machine learning in the vicinity of landmark points were considered, such as local texture features learnt by kNN classifer [14], and local SIFT features [15].

2.2. Initialization Stage

Given a test image, an initialization sufficiently close to the target contour is defined to approximate the object shape. This could be done by placing the mean shape $\overline{C}$ in the center of the test image with a user-guided transformation T, where T is a function of translation t, rotation θ, and scaling s of the mean shape as follows:

$$C^{(0)} = T(\overline{C}) = M(s,\theta)\overline{C} + t = \begin{bmatrix} x_j s \cos\theta - y_j s \sin\theta \\ x_j s \sin\theta + y_j s \cos\theta \end{bmatrix} + \begin{bmatrix} t_{x_j} \\ t_{y_j} \end{bmatrix} \quad (4)$$

The pose parameters θ, s, and t are chosen to ensure that the initial contour is reasonably close to the target shape. Several efforts have been made to automate the initialization [19-23].

2.3. Segmentation Stage

After an initial contour has been estimated, both shape model and GLAM generated in the learning stage are used for segmentation. For example, in a test image, best matches are made using GLAM to find the desired displacement (dC) for each landmark point (See Fig. 2). The corresponding adjustments to both the pose parameters ($d\theta$, ds, (dt_x, dt_y)) and shape parameters (db) are then calculated within the constraints of b. This process is iterated until little change is seen along all landmark points. More details about this

stage can be found in[18]. Note that the search strategy is to find the target point by only inspecting the local edge gradients along the normal direction of landmark point, which can easily trap the search in a local optimum instead of reaching a global optimum.

3. PROPOSED METHOD

As pointed out above, due to its local search scheme the performance of ASM relies on an initialization sufficiently close to the target. In this section, we present our global edge and region force (ERF) field based ASM (ERF-ASM) for lung field segmentation to address the limitations of typical ASM. The proposed method also applies PCA analysis to learn the lung fields' shape prior, which is then applied to regularize the later ERF-based segmentation. Our contributions compared to the typical ASM [18] include:

- Generating the initial shape automatically based on the global edge and region information.

- Applying a new point evaluation technique when locating the target contour of the lung field.

- Removing the constraint of placing initial landmark points sufficiently close to the target contour.

- Removing the constraint of manually adjusting the pose parameters.

The proposed procedure (Fig. 3) contains three stages: shape learning stage, automatic initialization stage, and segmentation stage. The novelty lies in the last two stages, which are described below.

3.1. Automatic Initialization Stage

In order to obtain accurate segmentation, a preliminary but crucial step is to estimate the pose parameters for automatic initialization. Different automatic initialization approaches for ASM [19-23] and their weaknesses have been discussed in the Introduction. Given the low contrast in chest radiographs, to achieve automatic initialization is a major challenge. In order to overcome the limitations of previous methods, we introduce Global Edge and Region Features Analysis into the Poisson Inverse Gradient (PIG) initialization process.

The PIG initialization method estimates the energy field from the force field that corresponds to the object shape in the image, and uses this estimated energy field to determine the most likely initial contour for the segmentation [25] (Fig. 4 illustrates the different energy and force fields). This automatic initialization is achieved in two steps.

Step 1 – Estimating the Energy from the Given Force by Solving Poisson's Equation

The PIG approach estimates the energy field E such that the negative gradient of E is the closest vector field to the force field $\mathbf{F}$ in the L2-norm sense. Then, the problem becomes:

$$E = \arg\min_{E} \iint \left| -\nabla E(x,y) - \mathbf{F}(x,y) \right|^2 dxdy \tag{5}$$

It can be shown that E is the unique solution of the following Poisson's equation:

$$\Delta E = -div\, \mathbf{F}(x,y) \tag{6}$$

where $\Delta = \dfrac{\partial^2}{(\partial x)^2} + \dfrac{\partial^2}{(\partial y)^2}$ is the Laplacian operator, and $div\, \mathbf{F} = \dfrac{\partial u}{\partial x} + \dfrac{\partial v}{\partial y}$ is the divergence of $\mathbf{F} =$

(u,v). In discrete domain (e.g., images), numerical methods are often applied to calculate E.

11

Step 2 – Selecting the Isomodel of the Estimated Energy for Initialization

After calculating the estimated E from $\mathbf{F}$, different isovalues of E with contours of isolines can be achieved. Those isolines are candidate isomodels. Since the final result in Snake's evolution is usually expected to correspond with image edges, an ideal initial contour should be close to those edges. Thus given an edge force, the isomodel with the lowest energy is chosen as the optimal initial contour. However, using edge force alone can lead to an inaccurate initialization as explained below. To address this issue, we perform three steps in our procedure.

Step 2.1 – Optimal Edge and Region Map Generation

In this step, an edge map B and a region map R are generated for the lung field. Since the chest radiographs are noisy, an edge-preserving and image smoothing scheme is necessary. We apply a speckle reducing anisotropic diffusion technique[26] for smoothing the image, preserving the strong edges, and suppressing speckle noise. The edge map B is then extracted using an edge detector, such as the Canny edge detector [27]. Fig. 4 (b) shows an example of the optimized edge map of the right lung image in Fig. 4 (a).

The region map R is generated by using a two-region segmentation technique in which the lung region is treated as the foreground and the rest of the image is treated as the background. Several region segmentation methods [28-30] were evaluated in our experiments, and it was found that the expectation maximization (EM) method proposed in [30] provides the best performance. Hence, in this work, we use EM technique to achieve optimal region map R. Fig. 4 (c) shows the region map corresponding to the image shown in Fig. 4 (a). Note that the broken contour in the edge map (Fig. 4 (b)) is enclosed after applying region information.

Step 2.2 – ERF Field Calculation

The edge and region field vector $\mathbf{f_{ERF}}$ is calculated by a linear combination of diffused edge force field $\mathbf{f_E}$ and diffused region force field $\mathbf{f_R}$ as follows:

$$\mathbf{f_{ERF}} = \lambda\, \mathbf{f_E} + (1-\lambda)\, \mathbf{f_R}, \tag{7}$$

where the parameter $\lambda \in (0,1)$ controls the relative weight of $\mathbf{f_E}$ and $\mathbf{f_R}$ in $\mathbf{f_{ERF}}$.

The edge force is the gradient of the image's edge map B. We adopt the gradient vector flow (GVF) technique proposed by Xu et al. [31] to globally diffuse the edge force field. The GVF field $\mathbf{g} = (u(\text{x,y}),v(\text{x,y}))$ is defined by minimizing the energy functional:

$$E_{ext} = \underset{\mathbf{g}}{\arg\min} \iint \eta(u_x^2 + u_y^2 + v_x^2 + v_y^2) + |\nabla B|^2 \cdot |\mathbf{g} - \nabla B|^2 \, dxdy \tag{8}$$

where η is the smoothing factor, and ∇B is the gradient of the edge map B. Using variational calculus, the GVF field can be found by solving the Euler equations of Eq. (8). Finite difference approach is then applied to achieve its numerical solution on a discrete grid. Fig. 4 (d) shows the diffused edge force field of the chest radiograph given in Fig. 4 (a).

The diffused region force field is generated similarly with an assumption that the gradient of the optimal region map R is the region force field. Fig. 4 (e) shows the diffused region force field of the example chest radiograph, and Fig. 4 (f) is our final ERF vector field after combining the global edge and region force fields.

Step 2.3 – Initialization using global edge and region features

PIG-based method was reported in [25] to be more efficient than other automatic initialization techniques. However, using edge force alone in the PIG method can lead to an inaccurate initialization result. For example, the isoline passing through the gap between broken edges will result in an inaccurate initialization (Fig. 4 (h) & (j)). Therefore, we introduce region force and mean shape alignment to obtain better results. We perform two processes as follows:

First, we replace the edge force with our ERF field. Thus, the Poisson Eq. (6) becomes:

$$\Delta E = -div\, \mathbf{f}_{\mathbf{ERF}}(x, y) \tag{9}$$

For example, given the ERF field in Fig. 4 (f), the estimated energy field by solving Eq. 9 is shown in Fig. 4 (g). In the next step, a mean shape alignment is then applied to achieve the final optimal initialization. The mean shape, which we derived from the shape learning stage, is placed in the middle of the image, and each landmark point on the mean shape seeks its corresponding point on the isoline obtained from the previous step. The optimal initialization is achieved by minimizing the distance between the mean shape and the isoline. All the corresponding points will gradually form an approximate shape, and the initialization is eventually finished by aligning the mean shape with this approximate shape. Fig. 4 (i) & (k) shows our automatic initialization result of the example image, and Fig. 4 (h) & (j) are the result of the original PIG approach. Note that our result preserves a smoother and more accurate lung field contour.

3.2. Segmentation Stage

We introduce a new point evolution equation (PEE), which applies the global ERF field generated in the initialization stage, to lead the landmark points out of the local optima. Xu et al. [32] introduced the

GVF field **g** into the ASM's points evolution. Their PEE, including a given step size w and an annealing

factor k, is given as follows:

$$C = C^{'} + w \cdot k \cdot \mathbf{g}(C^{'}) \tag{10}$$

where C and C' denote the current and previous contours respectively, and the annealing factor $k = \dfrac{p}{t^q}$

(constants $p, q \geq 1$) decreases as the iteration time t increases.

Steered by both the direction and magnitude of **g**, this GVF-ASM improves the robustness and

accuracy of the segmentation. However, Eq. (10) has two limitations: first, the three parameters w, p and q

need to be chosen before searching for the target points and may need to be adjusted for different test

images; second, the lung contour in a chest radiograph is usually blurred, which means that the magnitudes

of the gradient vectors close to the contour edges change only slightly. But in Eq. (10) the power function

$1/t^q$ decreases too fast compared to the corresponding changes in the gradient vectors, resulting in an early

convergence. In order to reduce the complexity and improve the search accuracy, we propose a new PEE

below, based on our preliminary study published in[33], which can provide more stability and accuracy:

$$C = C^{'} + w \cdot \text{sgn}(\mathbf{g}(C^{'})) \cdot e^{-\left|\mathbf{g}(C^{'})\right|} \tag{11}$$

where sign function *sgn* keeps the GVF vector's direction and the function *exp*(-|**g**(C')|) works as a smooth

monotonically decreasing function (or a speed function), which attracts the points to edges along the lung

contour. Since the boundary of the lung field does not always correspond with continuous edges, we

improve the performance by incorporating both edge and region information of the lung fields. This is done

by substituting the GVF vector **g** with our ERF vector **f$_{ERF}$**. The final PEE is computed as:

$$C = C' + w \cdot \text{sgn}(\mathbf{f}_{\text{ERF}}(C')) \cdot e^{-|\mathbf{f}_{\text{ERF}}(C')|}. \tag{12}$$

We illustrate the difference between PEE (10) and (11) by both 1-D and 2-D force field examples. Fig. 5 shows point evolution guided by 1-D GVF field $\mathbf{g} = \{0.01, 0.02,..., 1, -1, -0.99,..., -0.01\}$. Note that $\mathbf{g}$ is a GVF field corresponding to 200 points position ($1 \leq x \leq 200$), and the strong edges lie at $x = 100$ (when $\mathbf{g} = 1$) and $x = 101$ (when $\mathbf{g} = -1$). The horizontal axes represent the iteration time t, and the vertical axes represent the landmark point's new coordinate x at different t. The graphs in Fig. 5 show the evolution of landmark point x over time t. Observe that in Fig. 5 (a) evolutions corresponding to both PEE (10) and (11) converge to the expected strong edges ($x = 100$ and $x = 101$) with parameters $w = p = q = 1$ for PEE (10) and $w = 1$ for PEE (11). However, in Fig. 5 (b), the evolution of landmark point using PEE (10) leads to an early false edge convergence with $w = q = 2$, $p = 1$, while the result of using our proposed PEE (11) is still accurate with $w = 2$. In other words, PEE (10) is sensitive to parameters selection.

Fig. 6 shows another example with a different 1-D GVF whose value changes more rapidly compared to the $\mathbf{g}$ considered in Fig. 5, $\mathbf{g} = \{0.01, 0.06,..., 0.96, -0.96, -0.91,..., -0.01\}$, where the strong edges lie at $x = 20$ (when $\mathbf{g} = 0.96$) and $x = 21$ (when $\mathbf{g} = -0.96$). It can be observed that the point evolution using PEE (10) has strong ringing effect, and jumps too far away from the strong edges position.

In the analysis depicted in Figs. 5 and 6, the proposed PEE is more accurate and stable; this can also be proved in the 2-D domain. Fig. 7 shows some evolution results of our point evolution process compared to Eq. (10).

After all the landmark points converge, the shape model's parameters are updated accordingly. The stopping criteria can be defined by the number of iterations or a threshold specifying the Euclidean distance

between two consecutive iterations. In the experiments, we used a fixed number of iterations.

4. PERFORMANCE EVALUATION

In this section, we compare the performance of our proposed method with the typical ASM [18] and LSSP[42].

4.1. Database Used and Lung Field Definition

Standard postero-anterior (PA) chest radiographs from two different databases (normal and abnormal) are used in our experiments: (1) a publicly available Japanese Society of Radiological Technology (JSRT) database [34]; (2) a chest X-ray (CXR) image database from the University of Alberta Hospital. The JSRT database contains 93 normal PA-view images with resolution of 2048×2048, and the CXR image database has 50 pulmonary tuberculosis PA-view images with different resolutions.

We downsample the images in the JSRT database to 512×512 pixels and images in our CXR database to approximately 512×512 due to the following reasons: First, in our experiments 512×512 is a suitable resolution agreed to by radiologists to be adequate for them to define ground truth and perform visual assessments. Second, for computational efficiency it is common to segment the lung field in lower resolution, as an initial screening step and then analyze higher resolutions if necessary. For example, Refs. [9][14][15][42] use 256×256, and Refs. [11][16] use approximately 512×512.

We define the lung field as the part of the chest radiograph which contain lungs not obscured by diaphragm, mediastinum and heart[35]. A professional radiologist helps to manually draw lung field contours for both test and training images using a mouse cursor on an interactive interface.

4.2. Parameters Configuration

Parameters in our proposed method are set as follows: in the shape learning stage, for images from the JSRT database, we use an aligned training set of M = 23 left or right lung field contours, annotated with N = 30 landmark points. Twelve principal component vectors, which represent 90% of the total variance of the training set, are used to model the shape variation of the aligned lung field training set. We apply a similar process for our CXR database with fewer chest radiographs, M = 20, N = 30. In the automatic initialization stage, the smoothness factor η is set to 0.2 empirically following previous research [31], and the optimal weight parameter λ of 0.6 in Eq. (7) is found to generate good results by a simulation experiment which will be explained in detail in Subsection 4.3. In the segmentation stage, the evolution step size w in Eq. (12) is fixed at 1, and the number of iterations is set to 100. Fig. 8 shows an example of the segmentation process.

As for the parameters in the comparative techniques of typical ASM[18] and hybrid LSSP [42], same parameters are followed in both training and initialization stages. In the segmentation stage of typical ASM, the length of searching profile along normal direction is selected as 19 pixels including the landmark point. In the segmentation stage of hybrid LSSP, after carefully tuning, the weight of shape related energy term β is set to 0.005, the smoothing parameter (weight of length term) λ is set to 0.1, and the balancing parameter of low level features w is set to 0.4. (β, λ and w are the same symbols used in [42].)

4.3. Experiments and Analysis

The automatic segmentation results of the test images are compared with ground truth data, which was manually outlined by a professional radiologist. By considering the problem as segmentation between lung and background, the performance of the proposed method is evaluated based on three indices: accuracy,

sensitivity and specificity [35], which are calculated as follows:

$$Accuracy = \frac{N_{TP} + N_{TN}}{N_{TP} + N_{TN} + N_{FP} + N_{FN}} \tag{13}$$

$$Sensitivity = \frac{N_{TP}}{N_{TP} + N_{FN}} \tag{14}$$

$$Specificity = \frac{N_{TN}}{N_{TN} + N_{FP}} \tag{15}$$

where N_{TP} is the true positive fraction (part of the image correctly classified as lung), N_{TN} is the true negative fraction (part of the image correctly classified as background), N_{FP} is the false positive fraction (part of the image incorrectly classified as lung), and N_{FN} is the false negative fraction (part of the image incorrectly classified as background). Another evaluation parameter for comparison between methods is the time-cost factor. It is defined as the curve evolution time based on the same initial contour to the same number of iterations. Our experimental platform is Matlab 2007b on an Intel Pentium 4 CPU 2.8G Hz with 2G RAM computer.

Following the above evaluation criteria, we designed two categories of experiments: (1) simulation experiments to determine the optimal weight parameter in ERF generation; (2) comparison experiments to evaluate segmentation results between hybrid LSSP technique [41], typical ASM technique [18] and our proposed global edge and region forced field based method.

The simulation experiment is performed by applying our ERF technique with variable λ on 20 chest radiographs which are randomly selected from our image database. The segmentation results of both left and right lung images are illustrated in Fig. 9 (a) and (b). We select $\lambda = 0.6$ to optimize accurate, sensitivity

and specificity.

The comparison experiments are applied to all the normal and abnormal images in our databases. The evaluation results are listed in Table 1. It is found that the proposed ERF method outperforms the typical ASM and LSSP techniques in average accuracy, sensitivity and specificity. For example, while the average accuracy of the left lung field segmentation in the JSRT image database is 91.7% using the typical ASM technique, the accuracy of the proposed method is 95.2%. The sensitivity and specificity also increase from 81.3% to 89.7% and from 95.9% to 97.2% respectively, which indicate that the proposed method has higher true positive rate and lower false positive rate. Considering both normal and abnormal left and right lung images, the proposed method provides around 4%, 6% and 3% overall improvement on the segmentation's accuracy, sensitivity and specificity, respectively. Similar improvement can be found by comparing the proposed method to hybrid LSSP technique. In addition, the standard deviations of the three evaluation criteria drop significantly when using the proposed method, suggesting our technique is more robust. As for the time-cost, LSSP is more than 800 times and typical ASM is more than 5 times than the proposed method, indicating our method is more efficient for real-time operation. Fig. 10 shows some segmentation results for comparison using the same initial contour for LSSP, ASM and our proposed method on both normal and abnormal left and right lung images. It can be observed that our proposed method gives more accurate results with respect to the ground truth. More examples of our proposed method are shown in Fig. 11 to give further impression on the performance.

The complexity involved in segmenting medical images varies depending on the anatomical structures. Lung field segmentation is challenging mainly because of the superimposed features, which blur the lung field region as well as create discontinuous edges along the contour. Although typical ASM techniques have

been proved to be successful in other types of segmentation, they have their limitations when applied to lung fields. Hybrid LSSP incorporating specific edge and region features improves the accuracy of lung field segmentation. However, due to the higher computational cost and more parameters needing to be tuned, our proposed technique is much more preferable than LSSP in real-time application.

5. DISCUSSION

Although many state-of-the-art segmentation methods, e.g., Generalized Hough Transform (GHT) and marginal space learning (MSL), have been proposed for medical imaging, they are often anatomy-specific and customized for the unique features in the image data [46-47]. The reason why lung field segmentation in CXR images continues to be challenging, compared to other anatomy, is because of complex contours, low contrast, more inhomogeneous regions, and superimposed anatomical structures. GHT is likely to fail when there is large variability of object shape or gray-level intensities[14]. GHT has several drawbacks such as computational expense given its vast global search, vulnerability to noise in edge orientation and location, and being fragile under rotation and scaling[48]. MSL is a recently proposed generic approach for segmenting anatomical structures in medical imaging modalities, such as CT and MRI[49]. It is a hierarchical, learning-based landmark classification technique. Following the marginal space learning paradigm, a series of probabilistic boosting tree (PBT) classifiers is used to estimate pose parameters (position, orientation and scale) at sequential stages. Haar-wavelet and steerable features are used separately for classification at each stage. One candidate is finally selected as the detected landmark. There are several concerns on using this technique. First, there is no priori information to ensure haar-wavelet and steerable features are optimal features for detecting lung field landmarks. Second, the

overlapping anatomical structures in chest radiograph and high variation of lung shapes in different patients can fail in accurate individual landmark detection.

Some commercial software for medical image analysis includes segmentation modules. For example, the famous MIPAV (Medical Image Processing, Analysis, and Visualization) system developed by NIH (http://mipav.cit.nih.gov/index.php) supports several segmentation methods such as fuzzy C-means, thresholding, geodesic active contour (GAC) level-set, watershed and so on. However, those methods are too general to achieve accurate results in specific applications such as lung field segmentation in 2D chest radiographs. We also tried out the Materialise's Mimics software (http://www.materialise.com/mimics) and could not obtain satisfactory result. In this paper, we propose to combine edge, region and shape information to produce more accurate lung field segmentation results.

6. CONCLUSIONS

In this paper we proposed an automatic global edge and region force (ERF) field guided method with non-linear exponential point evolution for lung field segmentation, by introducing global edge and force field information together with a new point evolution technique. Experimental results demonstrated that the proposed method is time efficient and improves the accuracy, sensitivity, specificity and robustness of the segmentation results, compared to the typical ASM and hybrid LSSP. Our automatic initialization also has better performance than the original PIG based initialization. Although we run our experiments on chest radiographs, the proposed ERF technique can easily be adapted to other image segmentation applications. Future developments include analyzing more complex ERF fields and other non-linear statistical shapes to improve the current model.

ACKNOWLEDGEMENT

APPENDIX

We conducted experiments to compare the ASM-based technique with LSSP. In this comparison we used a hybrid LSSP [42] which is more specific for lung field segmentation. In addition, we carefully selected the parameters in the new implemented LSSP detailed below.

Before discussing the parameters' selection, we first explain the difference between LSSP in [41] and [42], and why LSSP [42] is more specific for lung field segmentation.

The hybrid LSSP framework is based on the minimization of the following energy functional:

$$E = w_r E_{region} + w_b E_{boundary} + w_s E_{shape} \tag{16}$$

where w_r, w_b, w_s are the weights of three energy terms. The major differences between LSSP in [41] and [42] are the region and boundary energy terms. The comparison is listed in Table 2.

It can be seen that LSSP [42] is much more specific for lung field segmentation due to: (1) the incorporation of Gaussian distributions assumption of the inside and outside the contour in the region term, which is more precise than the homogeneity assumption in the CV model; (2) low level edge features including castrophenic angle corner feature are considered, which is more specific than the general image gradient.

Paper [42] simplifies the weights between edge, region and shape terms as $w_r = w_b = 1$, and only uses one parameter β to control the weight of shape term. Thus, three explicit parameters in LSSP [42] need to be decided: weight of shape term β, weight of length term (smoothing parameter) λ and low level edge feature balancing weight w. We first fix λ and w with appropriate values, tune β in the test of randomly selected 20 CXR images (See following Fig. 12 illustrating the results of tuning β). Based on the segmentation performance we find the optimal β. Then using this β, we fix w to find the optimal λ. Finally optimal w could also be decided. The final segmentation results shown in the revised paper are based on these optimal parameters. Note that the similarity coefficient of 0.86 in our LSSP implementation is consistent with the result (0.88) reported in [42]. This shows that the parameter value selection is not biased.

REFERENCES

[1]   Bağcı U, Bray M, Caban J, et al. Computer-assisted detection of infectious lung diseases: A review. Comput. Med. Imag. Graphics. 2012; 36(1):72-84.

[2]   Shiraishi J, Li Q, Appelbaum D, et al. Computer-aided diagnosis and artificial intelligence in clinical imaging. Semin. Nucl. Med. 2011; 41(6):449-462.

[3]   Ginneken BV, Romeny BMTH, Viergever M. Computer-aided diagnosis in chest radiography: a survey. IEEE Trans. Med. Imaging. 2001; 20(12):1228-1241.

[4]   McAdams HP, Samei E, Dobbins III J, et al. Recent advances in chest radiography. Radiology. 2006; 241(3):663-83.

[5]   Armato III SG, Giger ML, Ashizawa K, et al. Automated lung segmentation in digitized posteroanterior chest radiographs. Acad. Radiol.1998; 5:245-255.

[6]   Duryea J, Boone JM. A fully automated algorithm for the segmentation of lung fields on digital chest radiographic images. Med. Phys.1995; 22 (2):183-191.

[7]   McNitt-Gray MF, Huang HK, Sayre JW. Feature selection in the pattern classification problem of digital chest radiograph segmentation. IEEE Trans. Med. Imaging. 1995; 14(3):537-547.

[8]   Shi Z, Zhou P, He L, et al. Lung segmentation in chest radiographs by means of Gaussian kernel-based FCM with spatial constraints. Proc. FSKD (3), 2009, 428-432.

[9]   Brown MS, Wilson LS, Doust BD, et al. Knowledge-based method for segmentation and analysis of lung boundaries in chest X-ray images. Comput. Med. Imag. Graphics. 1998; 22:463-477.

[10] Park M, Wilson LS, Jin JS. Automatic extraction of lung boundaries by a knowledge-based method. Visual Information Processing. 2001; 2:14-19.

[11] Luo H, Gaborski R, Acharya R. Automatic segmentation of lung regions in chest radiographs: a model guided approach. ICIP. 2000; 2:483-486.

[12] Iglesias I, Tahoces PG, Souto M, et al. Lung segmentation on postero-anterior digital chest radiographs using active contours. LNCS. 2004; 3138:538-546-.

[13] Yu T, Luo J, Singhal A, et al. Shape regularized active contour based on dynamic programming for anatomical structure segmentation. Proc. of SPIE Med. Imag.: Image Processing. 2005; 419-430.

[14] Ginneken BV, Frangi AF, Staal JJ, et al. Active shape model segmentation with optimal features. IEEE Trans. Med. Imag. 2002; 21 (8):924-933.

[15] Shi YH, Qi F, Xue Z, et al. Segmenting lung fields in serial chest radiographs using both population-based and patient-specific shape statistics. IEEE Trans. Med. Imag. 2008; 27(4):481-494.

[16] Iakovidis DK, Savelonas MA, Papamichalis G, Robust model-based detection of the lung field boundaries in portable chest radiographs supported by selective thresholding. Meas. Sci. Technol. 2009; 20:104019.

[17] Behiels G, Maes F, Vandermeulen D, et al. Evaluation of image features and search strategies for

segmentation of bone structures in radiographs using active shape models. Med. Image Anal. 2002; 6:47-62.

[18] Cootes TF, Taylor CJ, Cooper DH, et al. Active shape models: their training and application. Comput. Vis. Image Understand. 1995; 61 (1):38-59.

[19] Cootes TF, Taylor CJ, Lanitis A. Multi-resolution search with active shape models. ICPR. 1994; A:610-612.

[20] Brejl M, Sonka M. Object localization and border detection criteria design in edge-based image segmentation: automated learning from examples. IEEE Trans. Med. Imag. 2000; 19:973-985.

[21] Li H, Chutatape O. Boundary detection of optic disk by a modified ASM method. Pattern Recogn. 2003; 36:2093-2104.

[22] Mahoor MH, Abdel-Mottaleb M. Facial features extraction in color images using enhanced active shape model. FGR. 2006; 144-148.

[23] Cosio FA. Automatic initialization of an active shape model of the prostate. Med. Image Anal. 2008; 12(4):469-83.

[24] Gower JC. Generalized Procrustes Analysis. Psychometrika. 1975; 40:33-51.

[25] Li B, Acton ST. Automatic active model initialization via Poisson inverse gradient. IEEE Trans. Image Process. 2008; 17(8):1406-1420.

[26] Yu Y, Acton ST. Speckle reducing anisotropic diffusion. IEEE Trans. Image Process. 2002;

11(11):1260-1270.

[27] Canny J. A computational approach to edge detection. IEEE Trans. Pattern Anal. Mach. Intell.1986; 8(6):679-714.

[28] Pham D, Prince J. Adaptive fuzzy segmentation of magnetic resonance images. IEEE Trans. Med. Imaging. 1999; 18:737-752.

[29] Comaniciu D, Meer P. Mean shift: a robust approach toward feature space analysis. IEEE Trans. PAMI. 2002; 24(5):603-619.

[30] Manjón JV. Segmentación Robusta de Imágenes de RM cerebral. Ph.D. dissertation. Universidad Politécnica de Valencia, Valencia, Spain. 2006.

[31] Xu C, Prince JL. Snakes, shapes, and gradient vector flow. IEEE Trans. on Image Proc. 1998; 359–369.

[32] Xu Y, Giritharan B, Oh J. Gradient vector flow driven active shape for image segmentation. Proc. of International Conference on Multimedia & Expo., 2007; 2058-2061.

[33] Xu T, Mandal M, Long R et al. Gradient Vector Flow based Active Shape Model for Lung Field Segmentation in Chest Radiographs. Conf. Proc. IEEE Eng. Med. Biol. Soc., 2009; 1:3561-3564.

[34] Japanese Society of Radiological Technology. http://www.jsrt.or.jp/english.html.

[35] Ginneken BV. Computer-aided diagnosis in chest radiographs. Ph.D. dissertation. Utrecht Univ., Utrecht, The Nederlands. 2001.

[36] Matlab codes packages used in the experiments. <http://viva.ee.virginia.edu/downloads.html>, <http://www.mathworks.com/matlabcentral/fileexchange/10956-em-image-segmentation>, <http://www.cb.uu.se/~ingela/Teaching/ImageAnalysis/Snakes/asm.tar>, and <http://www.math.ucla.edu/~xbresson/code.html>.

[37] Leventon M, Grimson W, and Faugeras O. Statistical shape influence in geodesic active contours. CVPR2000; 316–323.

[38] Tsai A, Yezzi A, Wells W, et al. Model-based curve evolution techniques for image segmentation. CVPR2001; 463-468.

[39] Vese LA and Chan TF. A multiphase level set framework for image segmentation using the Mumford and Shah model. International Journal of Computer Vision, 2002; 50(3):271-293.

[40] Wang Y, Wang L, et al. Level set evolution with locally linear classification for image segmentation. ICIP 2011; 3361-3364.

[41] Xavier B, Pierre V and Jean-Philippe T. A variational model for object segmentation using boundary information and shape prior driven by the Mumford-Shah functional, International Journal of Computer Vision, 2006; 28(2):145-162.

[42] Annangi, P, Thiruvenkadam, S, et al. A region based active contour method for x-ray lung segmentation using prior shape and low level features. IEEE ISBR 2010; 892-895.

[43] McCarthy A. Computer-aided detection chest X-ray helps identify lung lesions. Medscape Today News Article, 2009 (ARRS 2009 Annual Meeting: Abstract 103).

[44] Fraioli F, Bertoletti L, et al. Computer-aided detection (CAD) in lung cancer screening at chest MDCT: ROC analysis of CAD versus radiologist performance, J. Thorac Imaging, 2007; 22(3): 241-246.

[45] de Hoop B, De Boo DW, Gietema HA,et al. Computer-aided detection of lung cancer on chest radiographs: effect on observer performance. Radiology. 2010; 257(2):532-40.

[46] Withey DJ, Koles ZJ. Three generations of medical image segmentation: Methods and available software. Int J Bioelectromag. 2007; 9:67-8.

[47] Elnakib A, Gimel'farb G, et al. Medical image segmentation: a brief survey. In Multi Modality State-of-the-Art Medical Image Segmentation and Registration Methodologies. Springer New York. 2011.

[48] Assheton P, Hunter A, A shape-based voting algorithm for pedestrian detection and tracking. Pattern Recognition. 2011; 44(5):1106-1120.

[49] Zheng Y, Georgescu B, Comaniciu D. Marginal space learning for efficient detection of 2D/3D anatomical structures in medical images, Inf. Process Med. Imag. 2009; 21:411-22.

AUTHOR BIOGRAPHIES

Tao Xu received his B. Eng and M. Eng in 2003 and 2006, respectively, from the Department of Biomedical Engineering at Zhejiang University, Zhejiang, P. R. China. He is currently a PhD student in the Department of Electrical and Computer Engineering at the University of Alberta, Edmonton, Canada. His research interests include Computer Vision and Biomedical Image Analysis.

Mrinal Mandal, SMIEEE, received his M.A.Sc and Ph.D in Electrical and Computer Engineering from the University of Ottawa, Canada. From 1989 to 1992, he worked as a scientist in Indian Space Research Organization, Ahmedabad, India. He is currently a Full Professor and Associate Chair in the Department of Electrical and Computer Engineering, and Director of the Multimedia Computing and Communications Laboratory at the University of Alberta, Edmonton, Canada. His current research interests include Image and Video Processing, Storage and Retrieval of Images and Video, Medical Image Processing, Wavelets and VLSI architecture. He has a USA patent on lifting wavelet transform architecture. He was the Principal Investigator of projects funded by the Canadian Institute for Telecommunication Research (CITR), and the Federal Center of Excellence on Microelectronics Network (MICRONET). He is currently the Principal Investigator of a project funded by the Natural Sciences and Engineering Research Council of Canada (NSERC). He is a Member of IEICE, SPIE, IASTED, and registered Professional Engineer in the province of Alberta, Canada. He was a Canadian Commonwealth Fellow from 1993 to 1998, and an Alexander von Humboldt Research Fellow from 2005-2006. More details about his work can be found at http://www.ece.ualberta.ca/~mandal/.

Richard Long is currently a Professor in the Pulmonary Division of the Department of Medicine and an Adjunct Professor in the Department of Public Health Sciences, University of Alberta. He is also the Director of the Tuberculosis Program Evaluation and Research Unit of the Pulmonary Research Group, Department of Medicine, University of Alberta (http://www.ualberta.ca/~tbperu/). He is the immediate past Medical Officer of Health for Tuberculosis in the Province of Alberta (1998-2008); the immediate past Chair of the Canadian Tuberculosis Committee of the Public Health Agency of Canada and the immediate past Chair of the Tuberculosis Committee of the Canadian Thoracic Society. In these capacities he served as the Editor and Editor-in-Chief of the last two editions of the Canadian Tuberculosis Standards (http://www.publichealth.gc.ca/tuberculosis).

Irene Cheng, SMIEEE, is the scientific director of the Multimedia Research Group and an adjunct faculty in the Department of Computing Science, University of Alberta, Canada. Her research interests include computer vision, graphics, visualization and multimedia communication, especially in medical imaging and education applications. She has over 100 publications including two books and is the Chair of the IEEE NCS, EMBS Chapter; Board Member of the IEEE SMC Society, Human Perception in Vision, Graphics and Multimedia TC; a voting Member of the IEEE Communication Society, MMC TC; and the Chair of the 3D Rendering, Processing and Communications Interest Group.

Anup Basu, SMIEEE, received his Ph.D. in CS from the University of Maryland, College Park, USA. He originated the use of foveation for image, video, stereo and graphics communication in the early 1990s; an approach that is now widely used in industrial standards. He also developed the first robust (correspondence free) 3D motion estimation algorithm using multiple cameras (IJCAI'87), a robust (and the first correspondence free) active camera calibration method (CVPR'93), a single camera panoramic

stereo (ICPR'96), and several new approaches merging foveation and stereo with application to 3D TV visualization and better depth estimation. His current research applications include 3D/4D Image Processing and Visualization especially for medical applications, Multimedia in Education and Games, and Wireless 3D Multimedia transmission. He has been a Professor in the CS department at UofA since July 1999. He has also held the following positions: Visiting Professor, University of California, Riverside, 2003-2004; Guest Professor, Technical University of Austria, Graz, in 1996; Director, Hewlett-Packard Imaging Systems Instructional Lab., UofA, 1997 to 2000; and is currently an iCORE-NSERC Industry Research Chair.

TABLE 1. Segmentation methods evaluation using the same automatic initialization. Accuracy, sensitivity and specificity of different ASM methods on both left and right lung images of two image databases are used for the evaluation. The values of these three indices are represented by the average value ± standard deviation.

Database	Segmentation Method	Accuracy	Sensitivity	Specificity	Time Cost(s)
JSRT (Left Lung)	LSSP[42]	0.909 ± 0.020	0.857 ±0.047	0.931 ±0.028	320.18
	ASM[18]	0.917 ± 0.039	0.813 ± 0.083	0.959 ± 0.032	2.21
	Proposed	0.952 ± 0.013	0.897 ± 0.038	0.972 ± 0.014	0.38
JSRT (Right Lung)	LSSP[42]	0.913 ± 0.045	0.859 ± 0.061	0.944 ± 0.040	321.95
	ASM[18]	0.924 ± 0.034	0.847 ± 0.071	0.959 ± 0.035	2.38
	Proposed	0.955 ± 0.014	0.912 ± 0.030	0.976 ± 0.018	0.35
CXR (Left Lung)	LSSP[42]	0.910 ± 0.013	0.835 ± 0.090	0.943 ± 0.039	321.45
	ASM[18]	0.903 ± 0.034	0.825 ± 0.087	0.933 ± 0.038	2.37
	Proposed	0.946 ± 0.015	0.883 ± 0.050	0.969 ± 0.019	0.39
CXR (Right Lung)	LSSP[42]	0.924 ± 0.045	0.885 ± 0.086	0.947 ±0.036	320.22
	ASM[18]	0.899 ± 0.040	0.858 ± 0.085	0.912 ± 0.042	2.31
	Proposed	0.953 ± 0.017	0.900 ± 0.044	0.977 ± 0.020	0.33

TABLE 2. Comparison of Energy Terms between LSSP in [41] and [42].

	LSSP[41]	LSSP[42]
E_{region}	$\int_{\Omega_{in}} H(\phi)(\lvert I - u_{in}\rvert^2 + \mu\lvert\nabla u_{in}\rvert^2)d\Omega +$ $\int_{\Omega_{out}} (1 - H(\phi))(\lvert I - u_{out}\rvert^2 + \mu\lvert\nabla u_{out}\rvert^2)d\Omega$	$\int_{\Omega_{in}} H(\phi)((\frac{I - c_1}{\sigma_1})^2 + \ln(\sigma_1))d\Omega +$ $\int_{\Omega_{out}} (1 - H(\phi))((\frac{I - c_2}{\sigma_2})^2 + \ln(\sigma_2))d\Omega$
$E_{boundary}$	$\int_{\Omega} \delta(\phi)\lvert\nabla(\phi)\rvert g(\lvert\nabla I\rvert)d\Omega$	$\int_{\Omega} \delta(\phi)\lvert\nabla(\phi)\rvert(d_E^2 + \lambda)d\Omega$
where u_{in} and u_{out} are smooth approximations of the original image I in Ω_{in} and Ω_{out}. (c_1, σ_1) and (c_2, σ_2) are the parameters of the distributions inside and outside. H and δ are the Heaviside and Dirac functions, respectively. g is an edge detecting function. $d_E = wd_{E1} + d_{E2}$ denotes the sum of distance transforms of the Canny edge map d_{E1} and the castrophenic angle corner feature d_{E2}. μ and w are balancing weights. λ is the weight of length term.		
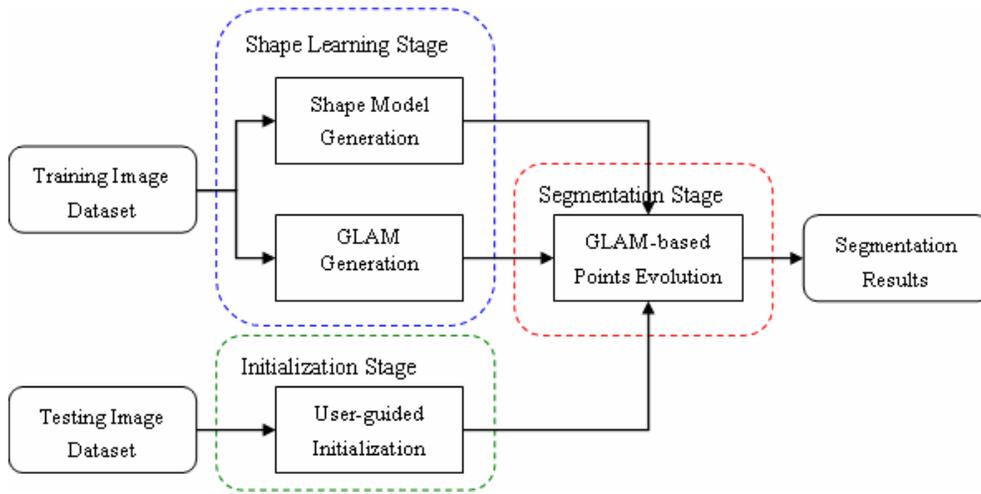
Fig.1. Major stages in a typical ASM segmentation process.
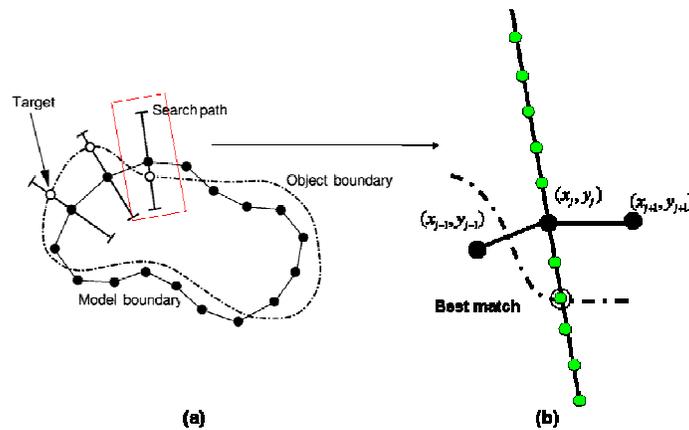
Fig.2. (a) In a typical ASM process, a landmark point moves towards the target point whose gradient profile

best matches the landmark point's GLAM. (b) A landmark point uses its searching profile to locate the best

matching target point.
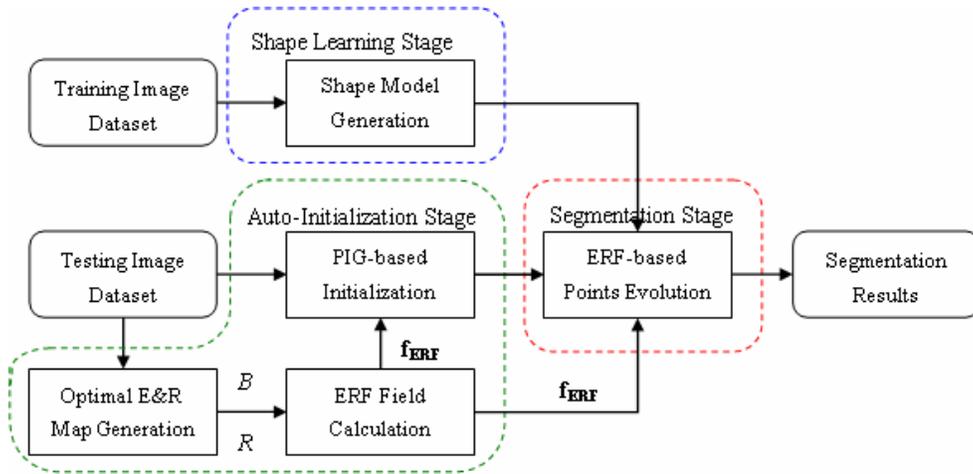
Fig.3. Our proposed automatic lung field segmentation procedure.

(a)   (b)   (c)

(d)   (e)   (f)

(g)   (h)   (i)

(j)   (k)
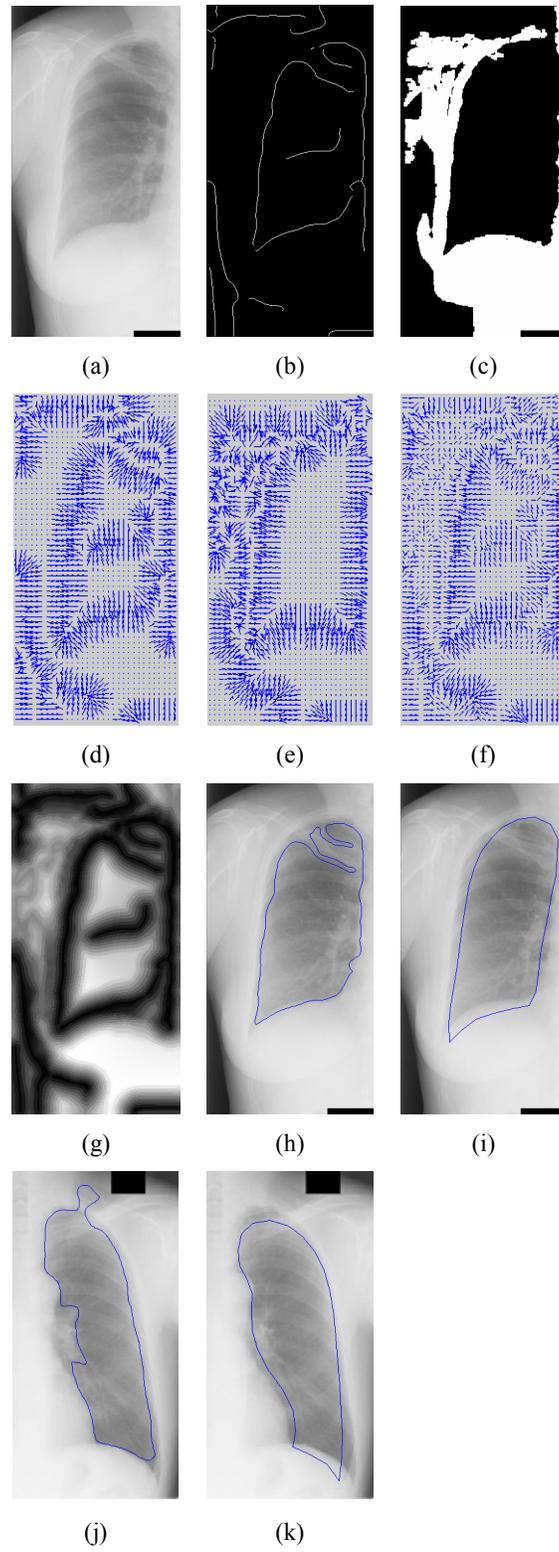
Fig.4. An example of our automatic initialization using edge and region force fields: (a) The original right

half lung image; (b) Optimized edge map B; (c) Optimized region map R; (d) Diffused edge force field $\mathbf{f_E}$; (e)

Diffused region force field $\mathbf{f_R}$; (f) Total ERF field $\mathbf{f_{ERF}}$; (g) Estimated energy field of the force $\mathbf{f_{ERF}}$; (h)

PIG-based initialization; (i) Our initialization. Another comparison is shown in (j) PIG-based initialization

and (k) our initialization.

(a)   (b)
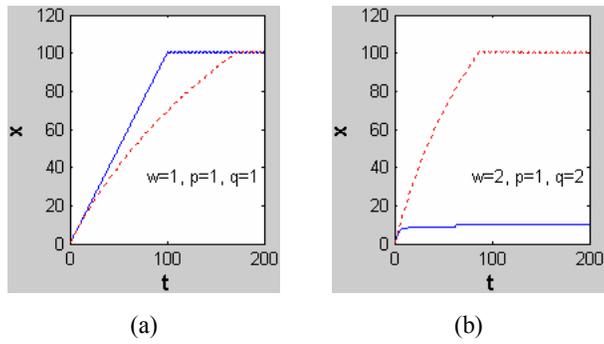
Fig.5. Example of 1-D point evolution using PEE (10) (solid line) and PEE (11) (dotted line). While both

converging to the strong edges in graph (a), the point evolution by using PEE (10) fails in graph (b) showing

that it is sensitive to even a small change in the parameter values.
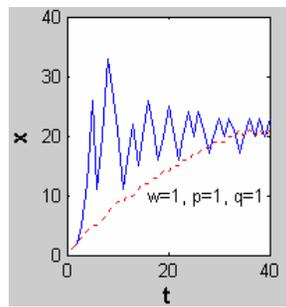
Fig.6. Another example of 1-D point evolution using PEE (10) (solid line) and PEE (11) (dotted line).

When changes are more rapid in a 1-D GVF field, point evolution using PEE (10) has strong ring effect

while the result of PEE (11) appears more stable.
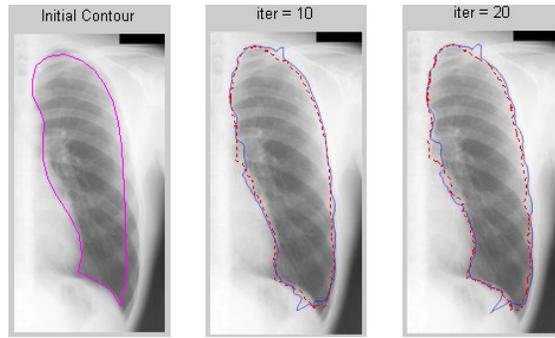
Fig.7. 2-D points evolution using PEE (10) with w=1, p=20, q=1 (solid line) and PEE (11) with w=1 (dotted line). The points evolution using PEE (10) jumps to some false edges at iteration time t = 10 and 20 comparing to the more accurate points evolution result of PEE (11).

(a)	(b)	(c)	(d)
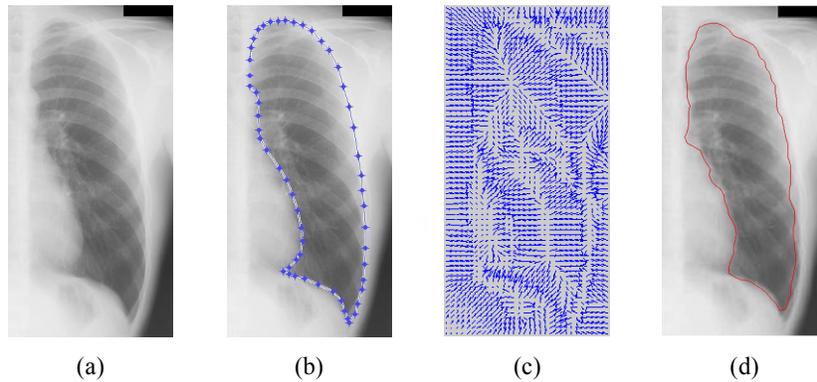
Fig.8. Performance of the proposed method for lung field segmentation: (a) left lung image; (b) ground truth; (c) generated ERF field; and (d) automatic segmentation result of proposed method.
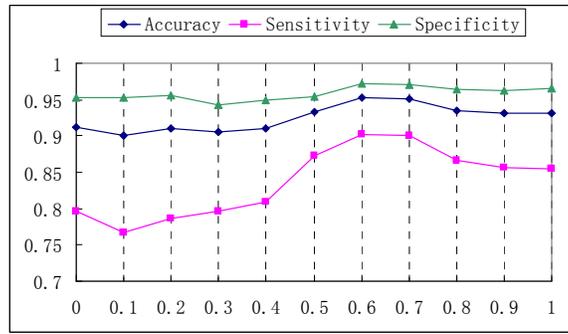
(a)
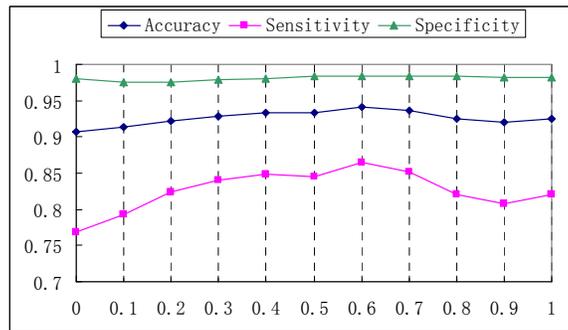
(b)

Fig.9. Simulation experiment with tuning weighted parameter λ in ERF generation where *x* axis stands for λ value changing from 0 to 1, and *y* axis is the average accuracy, sensitivity and specificity values over 20 randomly selected chest radiographs. (a) Results of 20 left lung images; (b) Results of 20 right lung images. We select $\lambda = 0.6$ to optimize accurate, sensitivity and specificity.

| Images | Ground Truth | LSSP | ASM | Proposed |
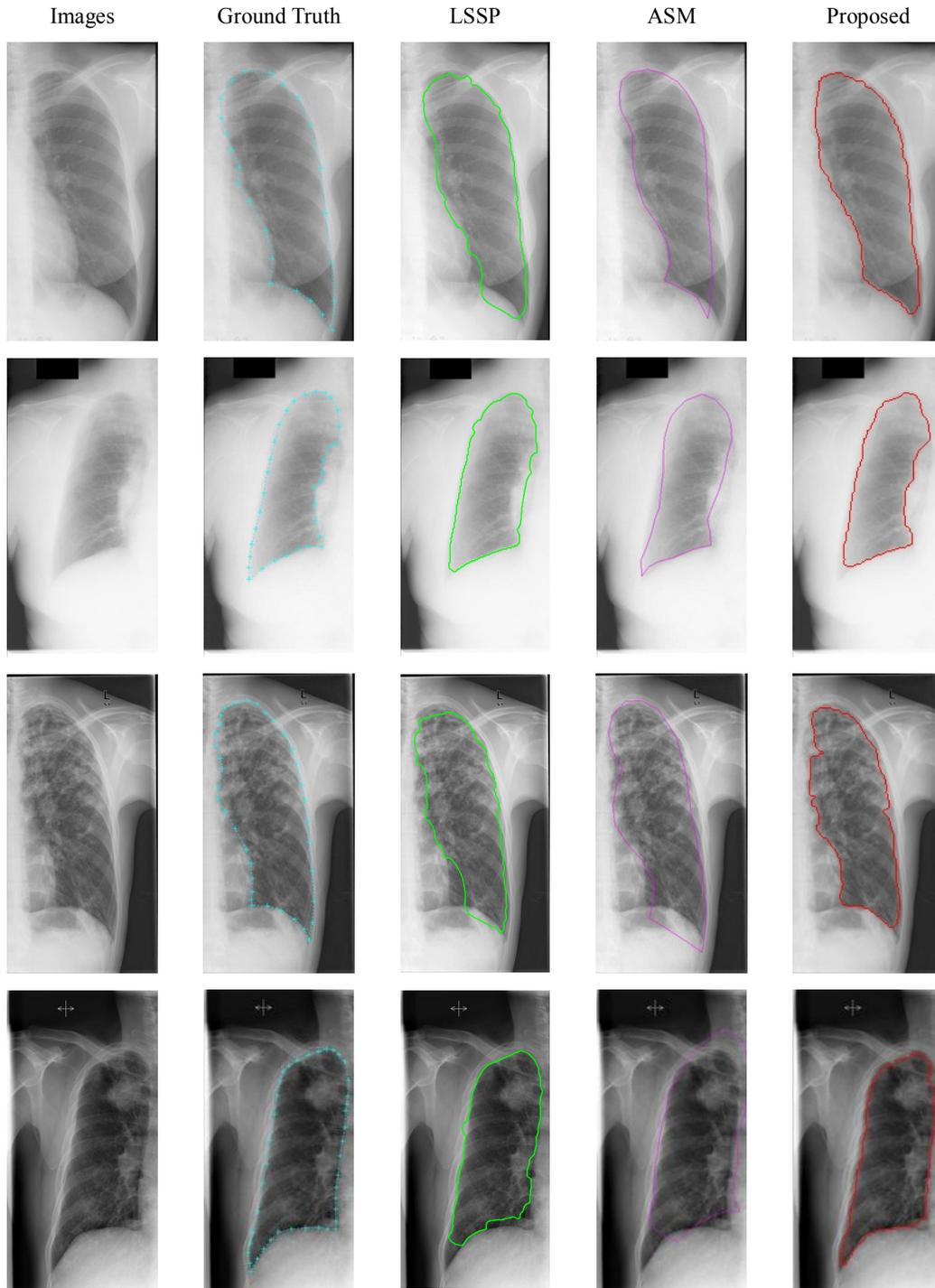
Fig.10. Comparisons of segmentation results, using the same initialization and ground truth, between LSSP,

typical ASM and our proposed on normal and abnormal images (both left and right lungs). Images from top

row to bottom row show normal left lung, normal right lung, abnormal left lung and abnormal right lung.
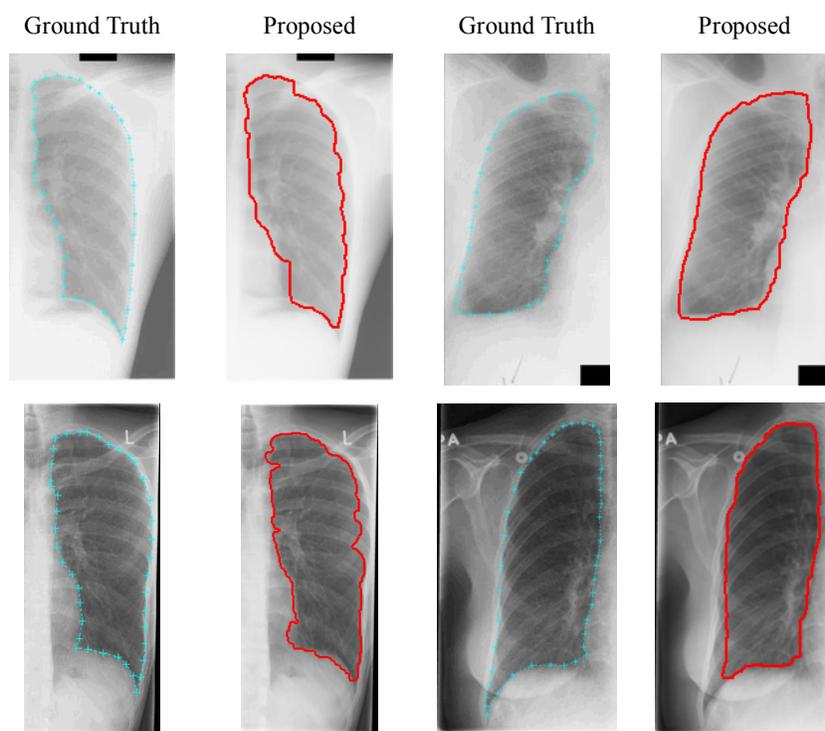
Fig.11. More examples of the segmentation results using our proposed method.
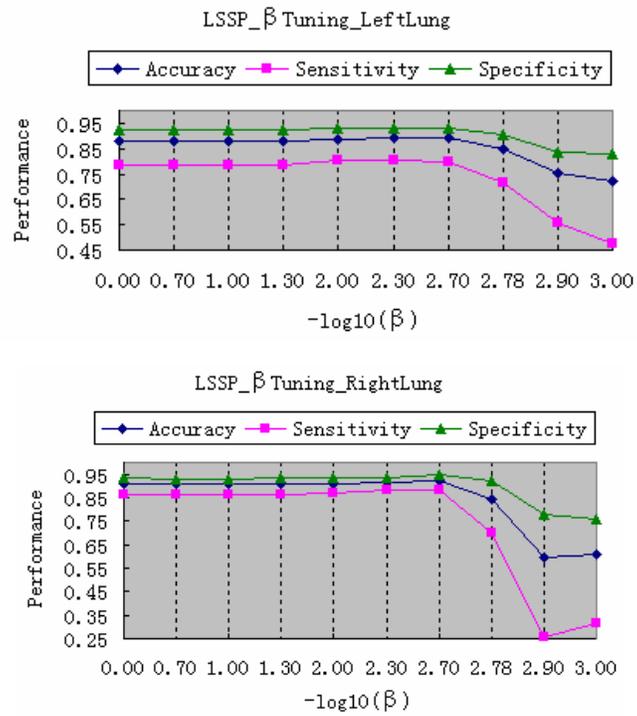
Fig. 12. Segmentation performance in 20 randomly selected CXR images with changing β and fixed λ

and w.